Electronic Supplementary Information

Post-synthetic modification of a highly flexible 3D soft porous metal-organic framework by incorporation of conducting polypyrrole: enhanced MOF stability and capacitance as electrode material

Zhen Li,[a] Julio Fraile,[a] Clara Viñas,[a] Francesc Teixidor,[a] José G. Planas*[a]

[a] Institut de Ciència de Materials de Barcelona (ICMAB-CSIC), Bellaterra, Spain.

E-mail: jginerplanas@icmab.es

EXPERIMENTAL SECTION

Materials. All chemicals were of reagent-grade quality. They were purchased from commercial sources and used as received. Pyrrole monomer (**Py**, C_4H_5N) was distilled before use. **1 ⊃ DMF** was prepared as previously reported.[1] Nickel foam was carefully cleaned by a 3 M HCl solution in an ultrasonicator and further washed with water and methanol for several times before using.

Preparation of 1 ⊃ PPy composite. 1 ⊃ DMF was firstly immersed into freshly distilled pyrrole monomer (**Py**) for three days at 4 ºC in a dark environment with the **Py** being exchanged once a day, to fully exchange the DMF in **1**. Excess of **Py** was removed and **1 ⊃ Py** crystals were rinsed with water and dried in air over a filter paper (Py per unit cell of **1** = 6). Then, dried **1 ⊃ Py** red crystals were immersed into an aqueous 0.2 M $K_2S_2O_8$ solution at 25 ºC in the dark for 24 h. The resulting black colored crystals were filtered and washed with water and methanol to yield the composite material **1 ⊃ PPy**.

Construction of the Electrode Materials [1 ⊃ A/NF@PPy; **A** = DMF or PPy**].**

In order to further facilitate the charge transfer and enhance the interactions between the MOF and the current collector, **1 ⊃ PPy** was directly grown on a PPy coated Nickel Foam current collector (NF@PPy).[2] This is to avoid using a polymer binder as this can significantly reduce the active interface and the equivalent series resistance of electrodes.[3] A piece of NF

(1x1 cm) was used as the working electrode (Figure S12). Silver and platinum electrodes were served as reference and counter electrodes, respectively. Electrochemical deposition of PPy on NF was performed in a N_2-saturated 1 M Na_2SO_4 aqueous solution containing 0.1 M pyrrole using the cyclic voltammetry technique within a potential window of 0-1.2 V at a scan rate of 50 mV S^{-1} for 10 cycles to provide NF@PPy (Figure S0**)**. Then, NF@PPy substrate was immersed in vertical position into a reaction vial containing the reaction mixture for synthesizing **1 ⊃ DMF**.[1] Crystals of the later grown on NF@PPy (**1 ⊃ DMF**/NF@PPy or **1/DMF**) were obtained after 20 h at 80 ºC. The later was thoroughly washed with DMF and water and dried on a filter paper at ambient conditions. Finally, DMF in **1/DMF** was exchanged by Py and further polymerized as described above to obtain the desired electrode material **1 ⊃ PPy/NF@PPy** or **1/PPy**.

Construction of the Electrode Materials [Py/NF@PPy**].**

A PPy/NF@PPy electrode was prepared in order to investigate the contribution of PPy formed by oxidation on the electrode. Firstly, the NF@PPy substrate, as prepared above, was immersed into the fresh distilled pyrrole solution for 3 days. After washing the electrode with water and dried on paper, it was further immersed into an aqueous 0.2 M $K_2S_2O_8$ solution at 25 ºC in the dark for 24 h. The as-obtained PPy/NF@PPy electrode was washed with water and methanol again before use.

Extraction of PPy from 1 ⊃PPy.

The **1 ⊃PPy** was immersed into a 5 M ammonium hydroxide solution for one week with the solvent being exchanged once a day. The as-obtained solid was further washed with water, DMF and methanol for several times to remove the residuals from the MOF. After repeating the above process once again, the final product of PPy was obtained and dried at ambient conditions on a paper.

Materials characterization.

Attenuated total reflection Fourier transformed infrared (ATR-FTIR) spectra were recorded in the range of 4000-400 cm^{-1} using a PerkinElmer Spectrum One spectrometer equipped with a Universal ATR sampling accessory. Thermogravimetric Analysis (TGA) was performed in N_2, on an NETZSCH -STA 449 F1 Jupiter instrument (heating rate: 10 ºC/min; temperature range: 25 ºC to 600 ºC). The content of the PPy in the composite was determined under air from 25 to 700 ºC with an increasing step of 10 ºC min^{-1} and then maintained at 700 ºC for another 30 minutes (this ensures the full combustion of PPy; Figure S3).[7] The N_2 adsorption–desorption

isotherms were measured on a Micromeritics ASAP 2460 analyzer. The samples were degassed under a high vacuum at 120 °C for 12 h prior to the measurements. The specific surface area was calculated with the Brunauer–Emmett–Teller (BET) equation, and the pore size distributions were calculated from the adsorption curve by the Barrett–Joyner–Halenda (BJH) method. The as-obtained powder samples and the electrodes at different cycling states were analyzed by X-ray powder diffraction (XRD, Siemens D-5000) with Cu-Kα radiation. The microstructure and morphology of the fabricated film electrodes were investigated by scanning electron microscopy (SEM) on a FEI Quanta 200 FEG microscope operating at 10 kV. Samples for SEM were coated with gold prior to measurement (high vacuum; sample to detector distance, 10 mm; spot 3.5). Nuclear magnetic resonance (NMR) spectra were obtained on a Bruker-Avance III 400SB equipment.

Electrochemical measurements.

Electrochemical measurements of all samples were conducted in a three-electrode system on an electrochemical workstation (Autolab potentiostat PGSTAT128N). 1 M aqueous Na_2SO_4 solution was used as the electrolyte. Pt and Ag/AgCl electrodes were served as counter and reference electrodes, respectively. The cycle voltammetry (CV) measurement was carried out within the potential window of 0-0.7 V with the scan rate varying from 5 to 50 mV/s. The galvanostatic charge−discharge measurements were also carried out at room temperature within the same potential range at different current densities from 4 to 10 mA/cm^2. The electrochemical impedance spectra were tested within the frequency range from 0.01 Hz to 100 kH with a sinusoidal signal of 5 mV. An equivalent electrical circuit and the ZSimpWin software were used to analyze the results. To evaluate the cycling stability of the electrodes, CV test was further performed at 5 mV/s for 500 cycles.

Based on the CV curves, the specific capacitances (C) of the electrodes can be calculated using the following equation:

$$C = \frac{\int I dV}{2 \times S \times \Delta V \times v} \qquad (1)$$

Where I (A) is the current density, ΔV represents the potential window (0-0.7 V), ν is the scan rate, and S is the apparent area of the working electrode (1x1 cm^2).[4, 5]

The C of the electrodes can also be calculated using the following equation based on the discharge curves:

$$C = \frac{I \times \Delta t}{S \times \Delta V} \qquad (2)$$

Where I (A) is the discharge current density, ΔV represents the potential windows, Δt (s) is the discharge time, and S is the apparent area of the working electrode (1x1 cm^2).[4, 6]

Figure S0. CV curves for electrochemical polymerization of pyrrole onto Nickel Foam matrix (**NF@PPy**).

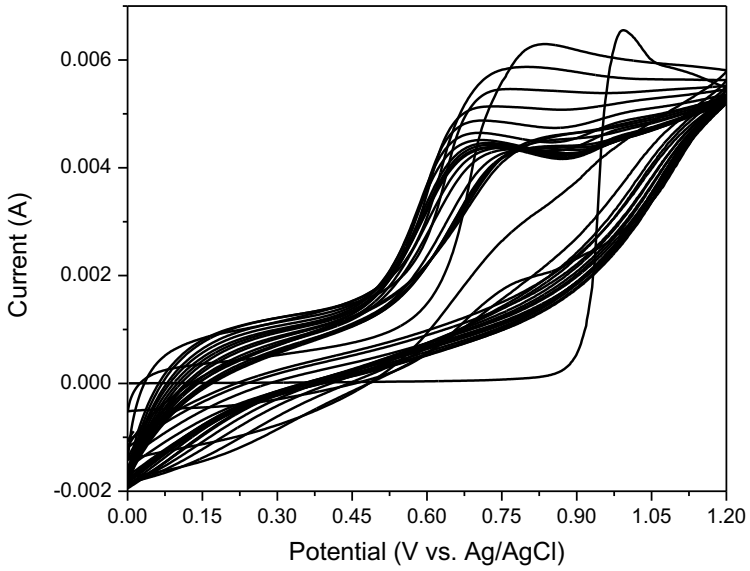

Figure S1. Comparison of IR data and optical microscope images for **1 ⊃ DMF** (orange)**, 1 ⊃ Py** (violet) and **1 ⊃ PPy** (blue). Bars in microscope images correspond to 100 μm.

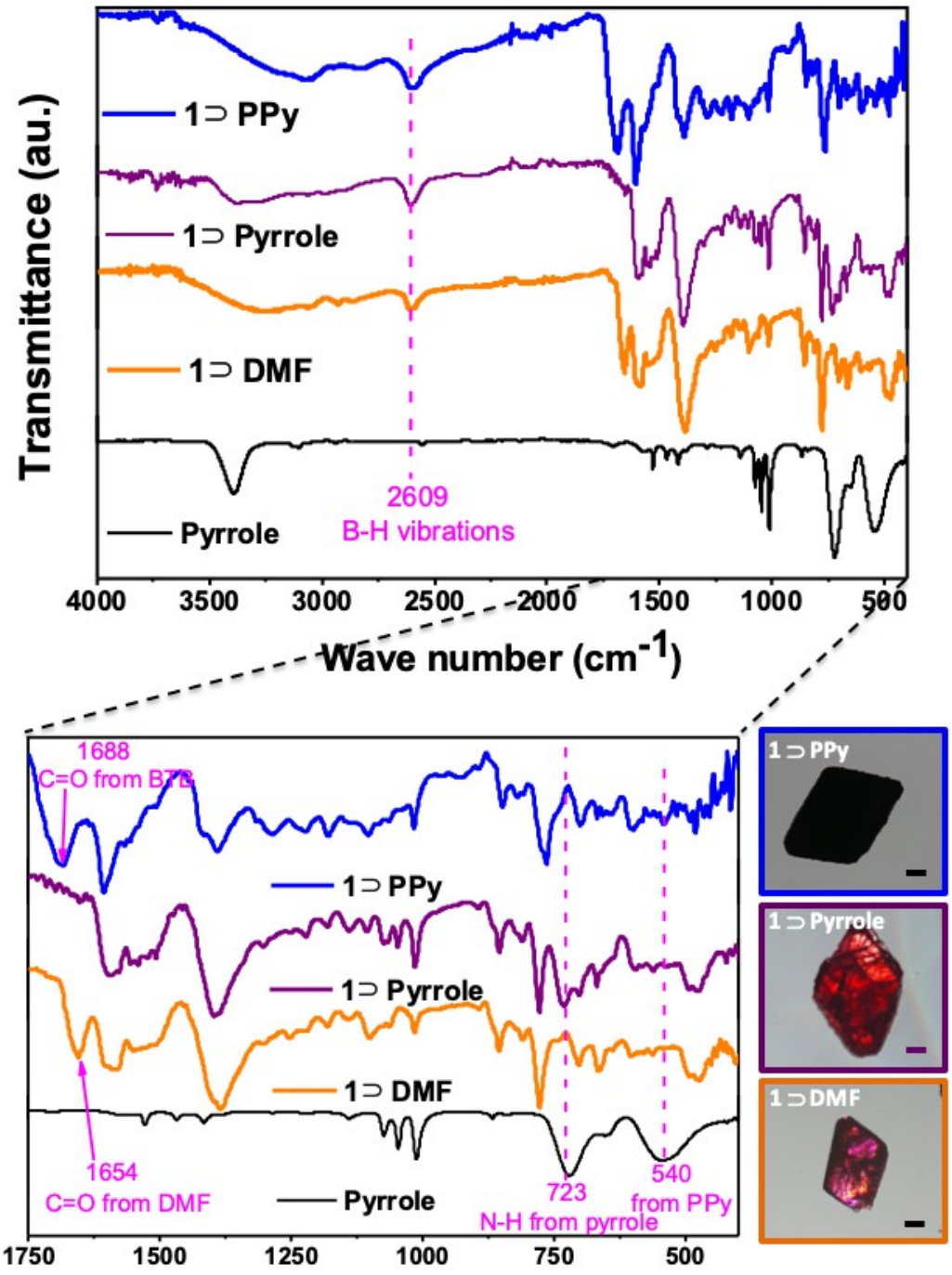

Figure S2. TGA curve of **1 ⊃ Pyrrole** tested under N_2 atmosphere.

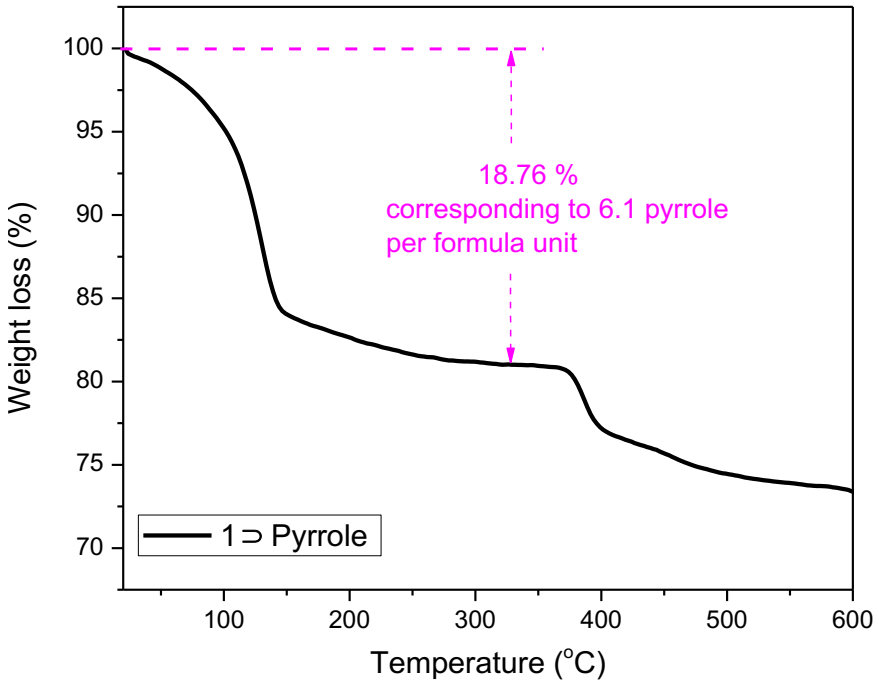

Figure S3. TGA curves of **1 ⊃ PPy** and **1 ⊃ DMF** under air.

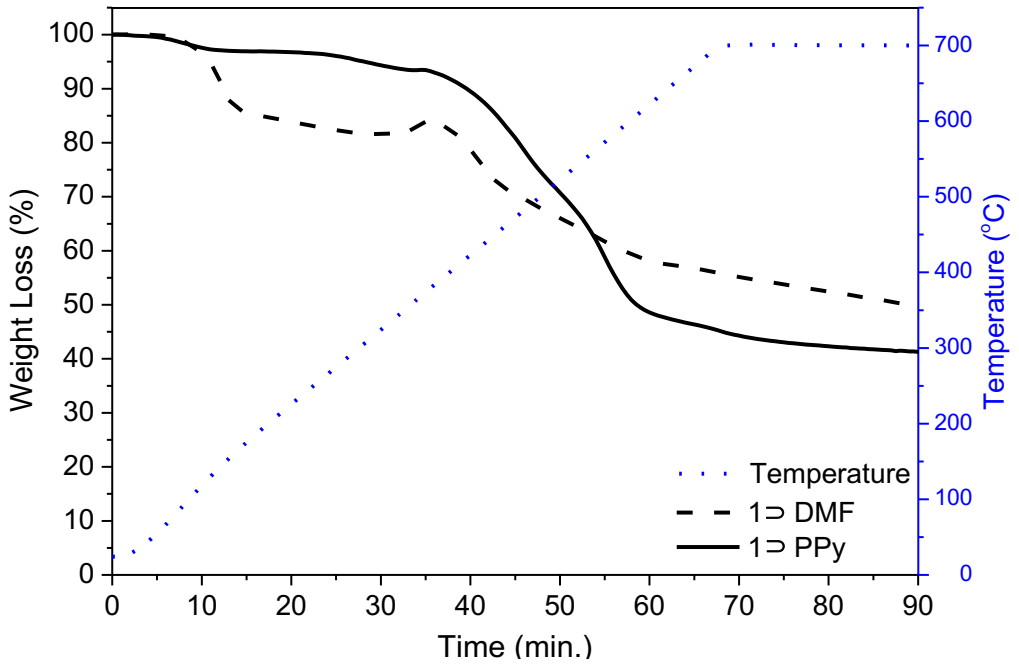

PPy content in **1 ⊃ PPy** was determined by TGA under air and in comparison with that for **1 ⊃ DMF** under the same conditions (Figure S3). Samples were heated up to 700 ºC and keep at this temperature for 30 minutes. The observed weight increase at 400 ºC is attributed to the oxidation of the carborane under the air atmosphere.[7] The heating conditions assures that all

PPy has been fully combusted.[8] The residue after full combustion of PPy (in wt%) corresponds to 45.1% (**1 ⊃ PPy**). The residue of **1 ⊃ DMF** at the same temperature and after correcting the contribution of free DMF is 60.94%. We therefore estimated a 26% loading of PPy in **1 ⊃ PPy** by using previously reported methodology (X_{PPy} (in wt% of the composite) = $1-r_{composite}/r_{MOF}$).[9]

Figure S4. Full PXRD spectra of **1 ⊃ PPy** and **1 ⊃ Py**.

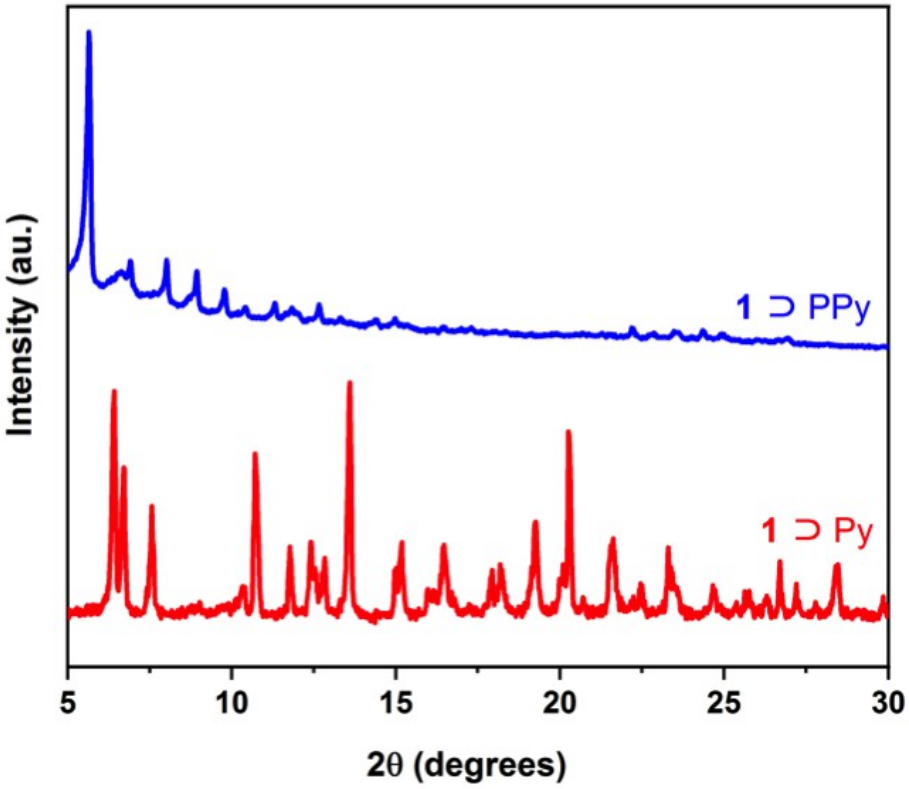

Figure S5. a) A representation of the crystal structure of **1** with (001) and (100) crystal planes indicated. b) Calculated PXRD patterns for **1** ⊃ **Solvent** (**Solvent** = Nitrobenzene, Toluene or Benzene) from the X-ray structures.[1]

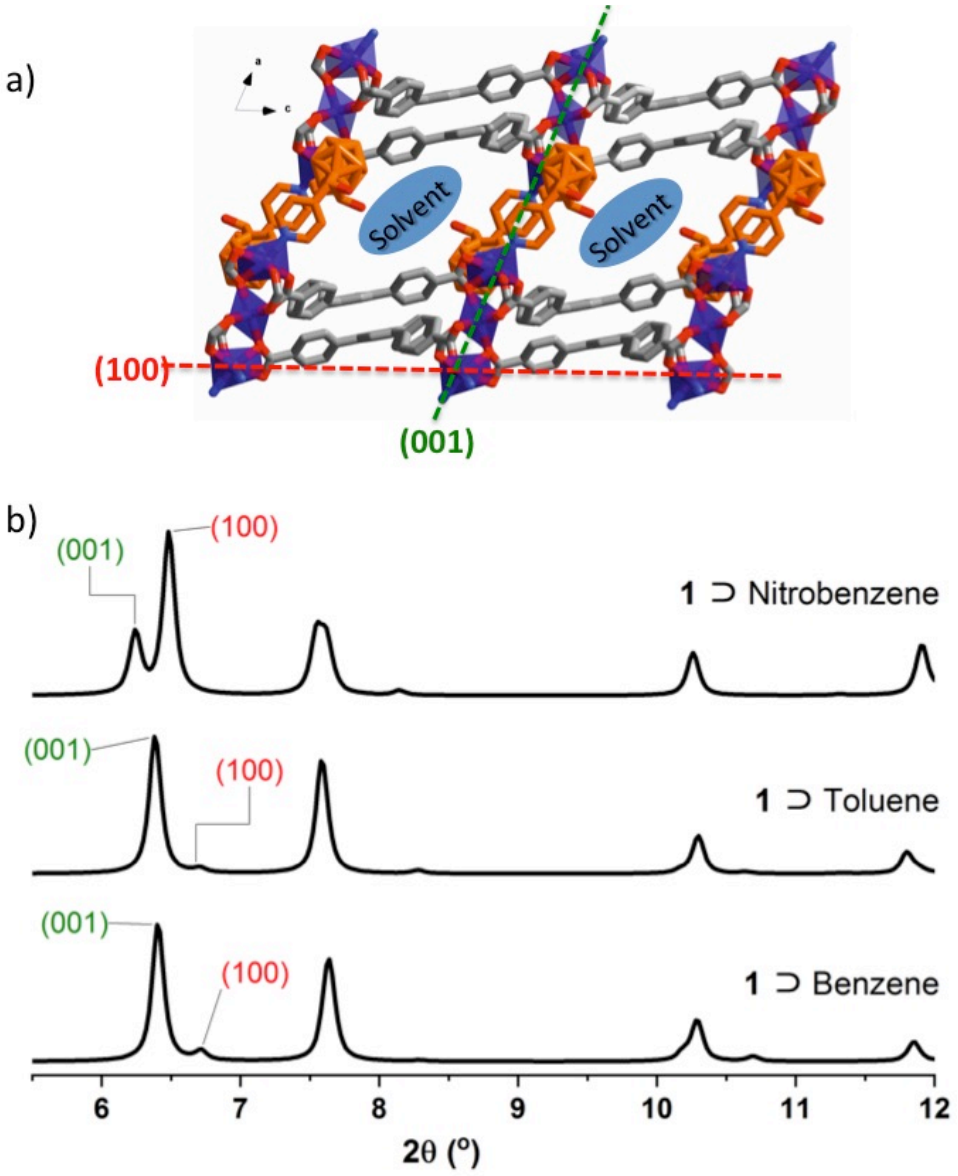

Table S1. Comparison of the diffraction peaks and interlayer distances for **1 ⊃ DMF**, **1 ⊃ Py** and **1 ⊃ PPy**.

Samples	Diffraction peaks (2Θ degrees)	Interlayer distances (Å)
1 ⊃ DMF	6.46	13.7
1 ⊃ Py	6.42	13.8
1 ⊃ PPy	5.64	15.6

Figure S6. Comparison of PXRD data for **1 ⊃ DMF** before (blue) and after (red) treatment with $K_2S_2O_4$ under polymerization conditions.

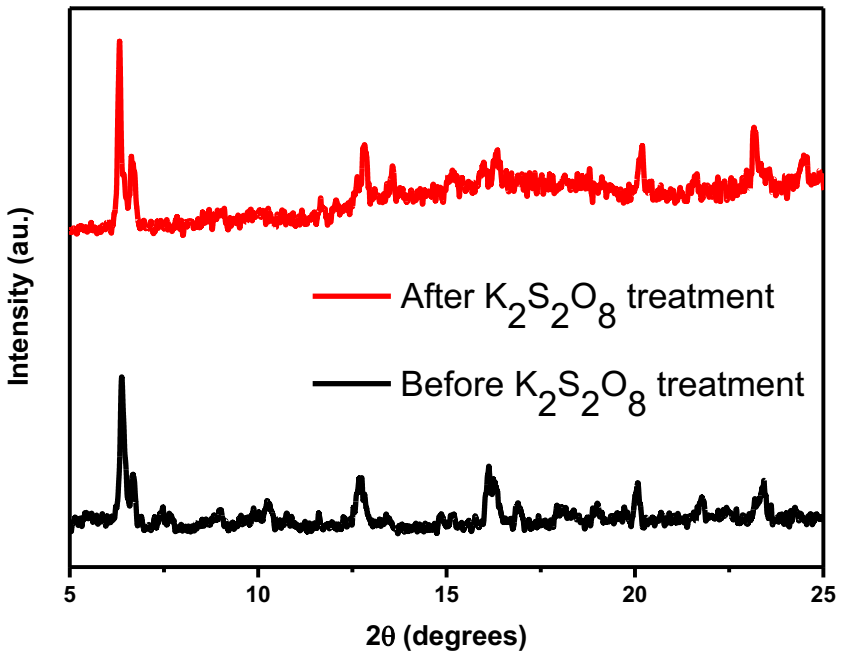

Figure S7. Scanning Electron Microscopy (SEM) images at various magnifications of **1 ⊃ PPy** before (**I**: 200, 500, 500, 5000 and 50000 magnifications) and after (**II**: 200, 500, 2000 and 5000 magnifications) ammonium hydroxide treatment.

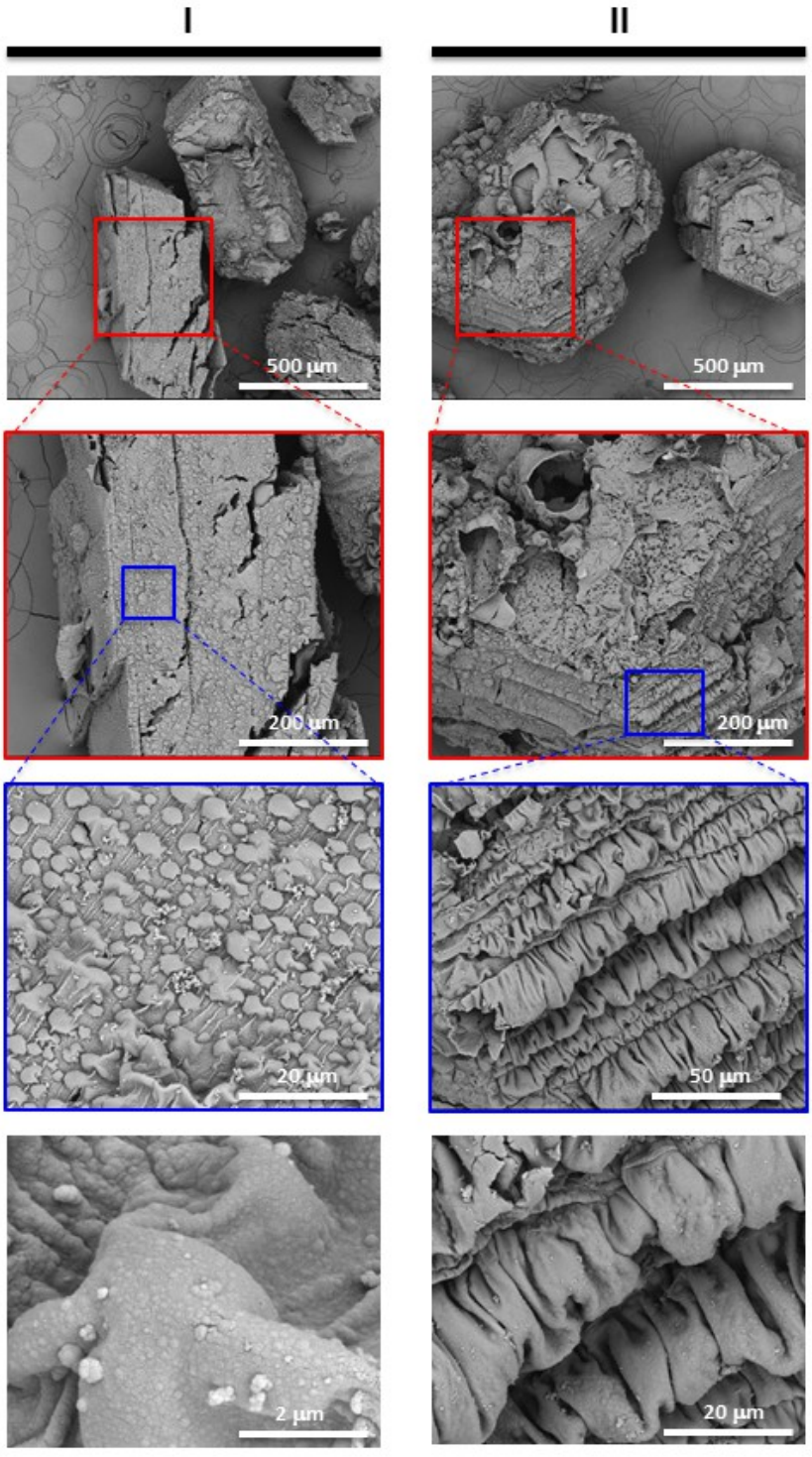

The treatment of the MOF composite with ammonium hydroxide allows the selective decomposition of the host MOF, resulting in polymer particles with a shape that replicated that of the crystals (Fig. S7-**II**). This results in systems constituted purely of polymer, that preserve

a degree of organization reminiscent of their history as a Polymer@MOF composite.[10,11] The images clearly show the distribution of PPy within the crystals. PPy is surrounding the crystal surface and embed layers withing the 1 ⊃ **PPy** composite.

Figure S8. Scanning Electron Microscopy (SEM) images at various magnifications of **1** ⊃ **PPy** after being crashed into pieces.

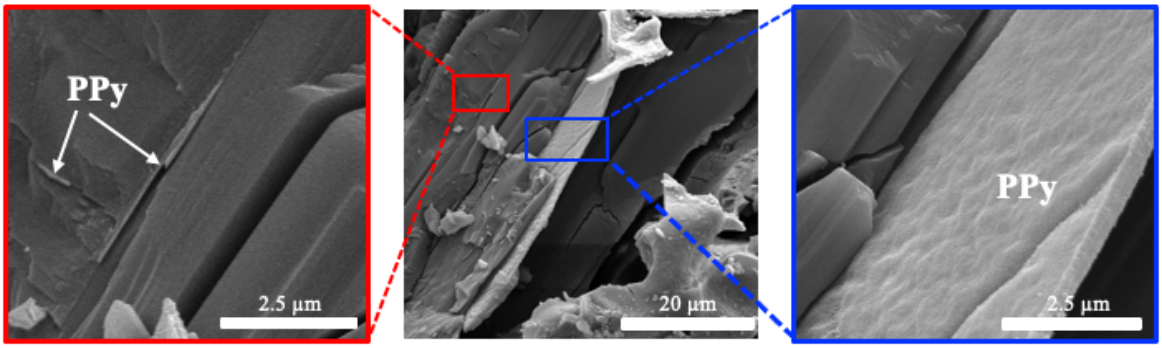

In order to further confirm that the PPy was impregnated within the MOF, we cracked the MOF ⊃ PPy composite and tested SEM (Fig S8). 2D PPy within the interlayers of the MOF can be clearly observed in the Figure. The visual proof provided by Fig S8 support the PXRD data for the composite that clearly shows that PPy is not only on the surface of the composite, but also within the interlayers of the MOF.

Figure S9. Scanning Electron Microscopy (SEM) image (A) and FTIR spectrum (B) of PPy isolated from 1 ⊃ **PPy**.

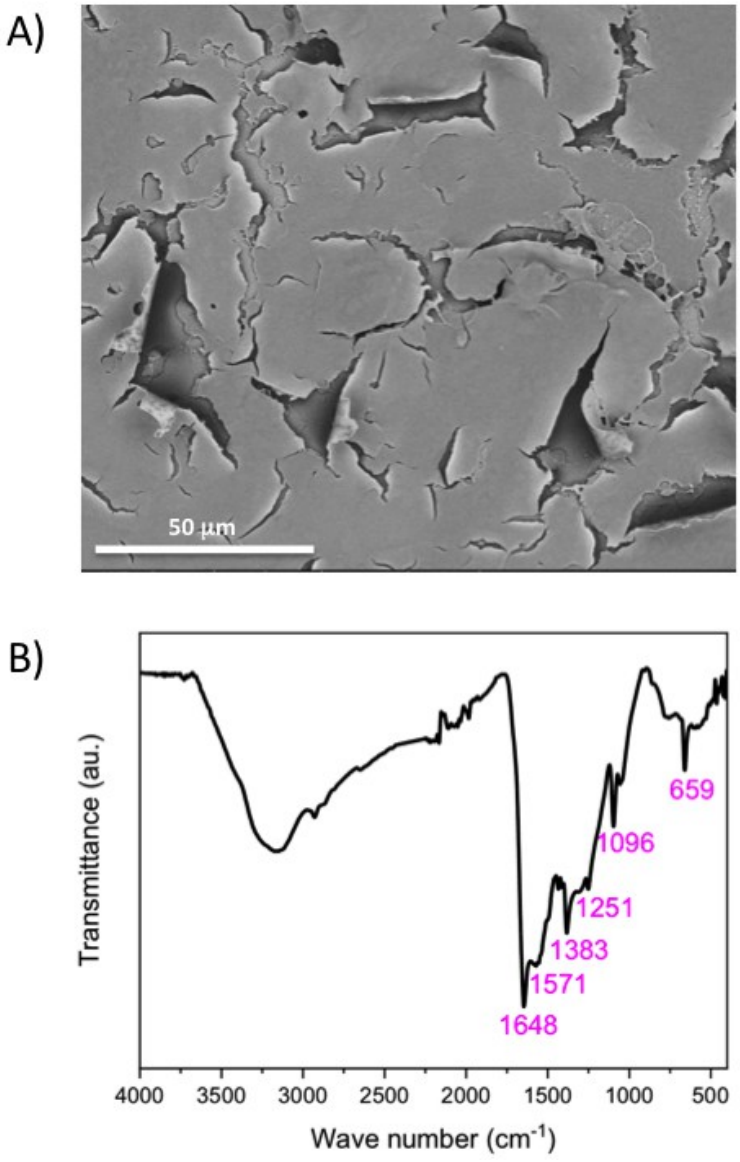

Figure S10. PXRD of **1** ⊃ **PPy** before (orange) and after (black) being in MeOH for 5 days and dried at 90 ºC.

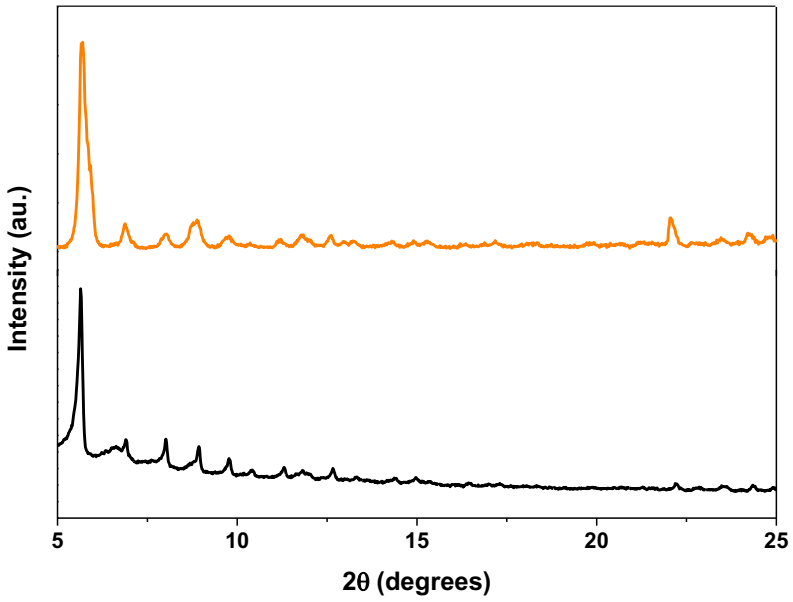

Figure S11. Pore size distribution (A) and PXRD (B) of **1 ⊃ PPy** before and after the BET measurement.

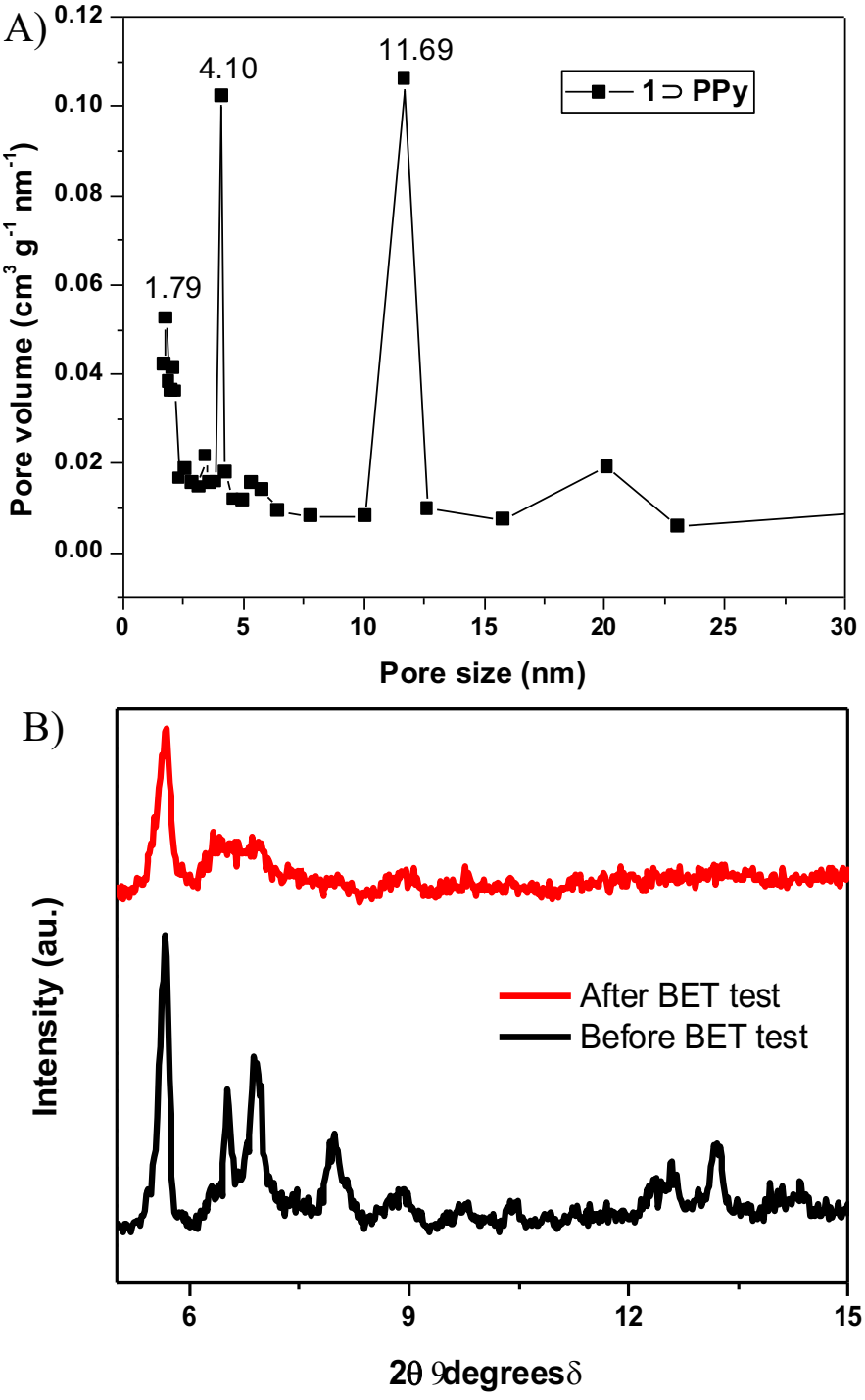

Figure S12. The experimental procedure for the preparation of **1/ DMF** electrode. **1 ⊃ DMF** growth is clearly improved on polypyrrole coated Nickel Foam (NF) as evidenced in the photos bellow. Not only a more homogeneous growth is observed but also the crystals do not detached after washing the electrode while shaking from the polypyrrole coated NF.

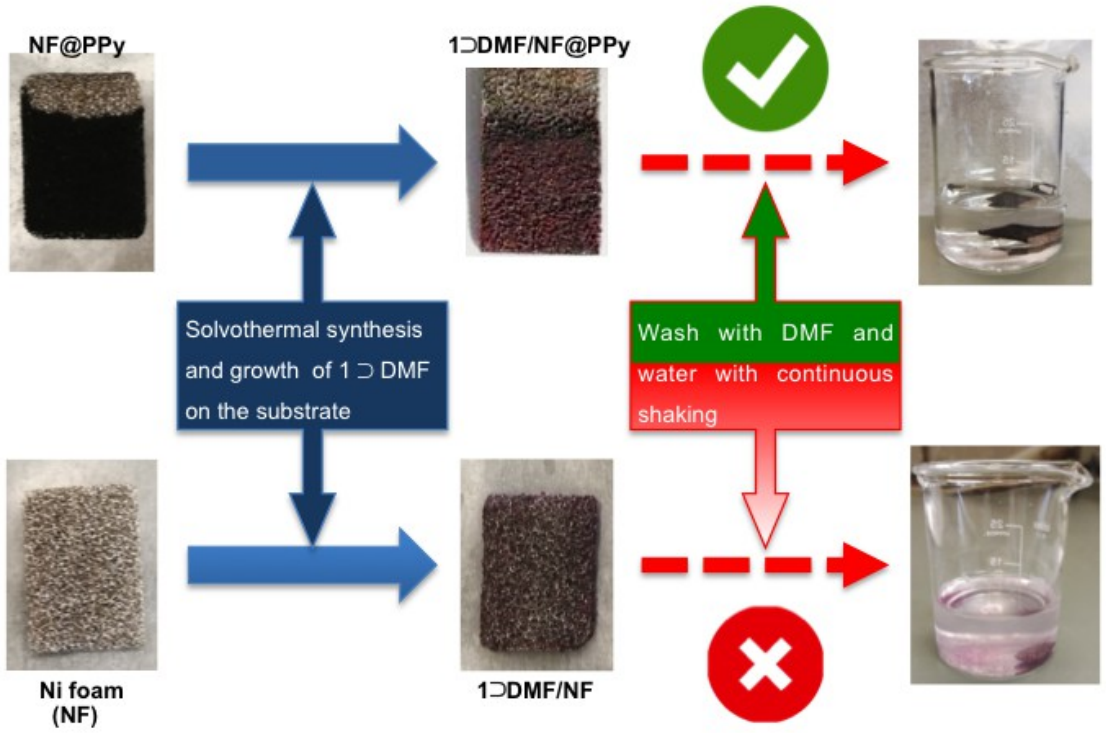

Figure S13. Optical images (top) and Scanning Electron Microscopy (SEM) images at various magnifications (bottom) of **1⊃DMF**/NF@PPy and **1⊃PPy**/NF@PPy electrodes.

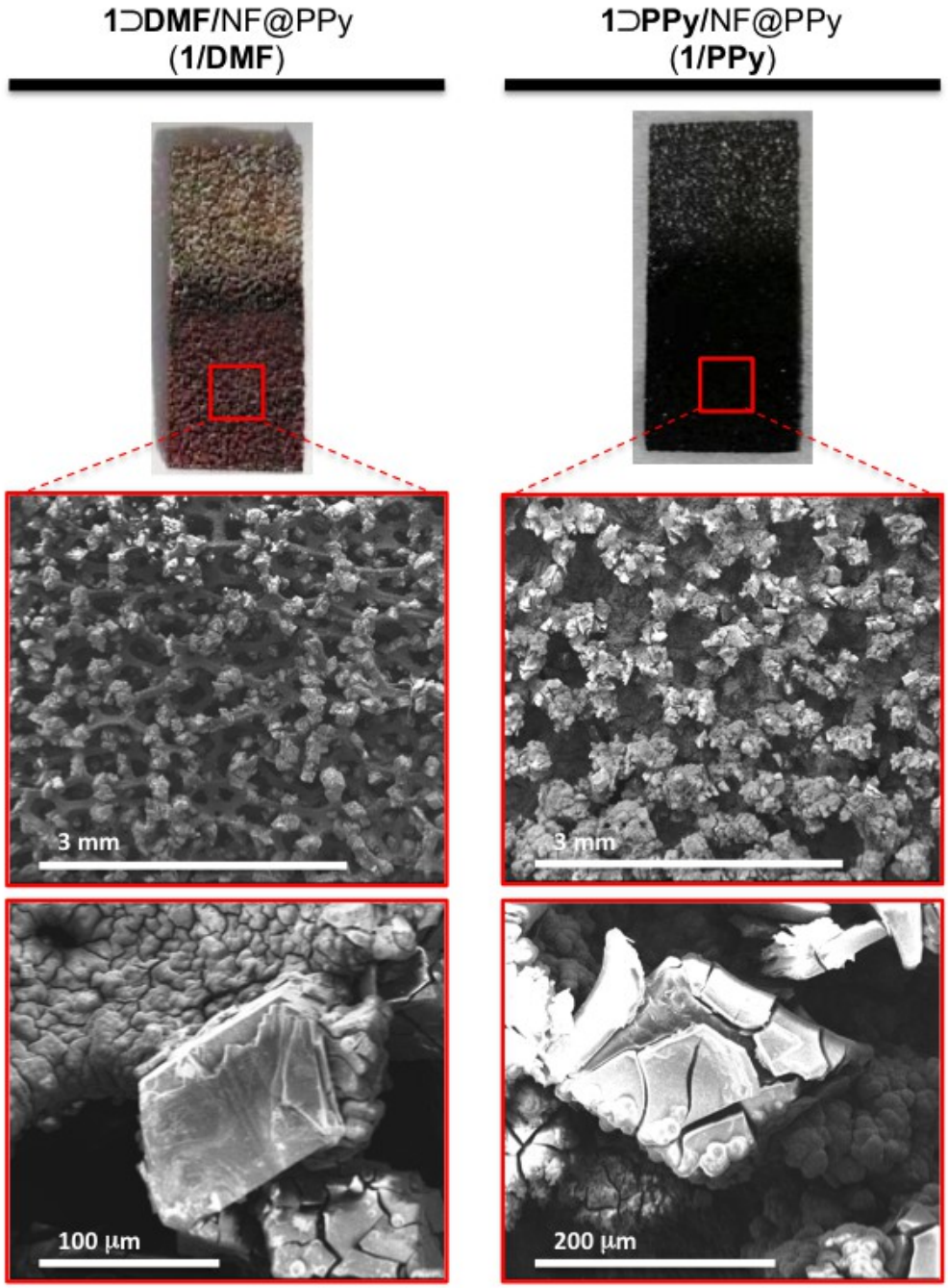

Figure S14. CV curves of **1 ⊃ PPy**/NF@PPy (A) and **1 ⊃ DMF**/NF@PPy (B) electrodes. GCD curves (C) and specific capacitance at various current densities (D) of **1 ⊃ PPy**/NF@PPy.

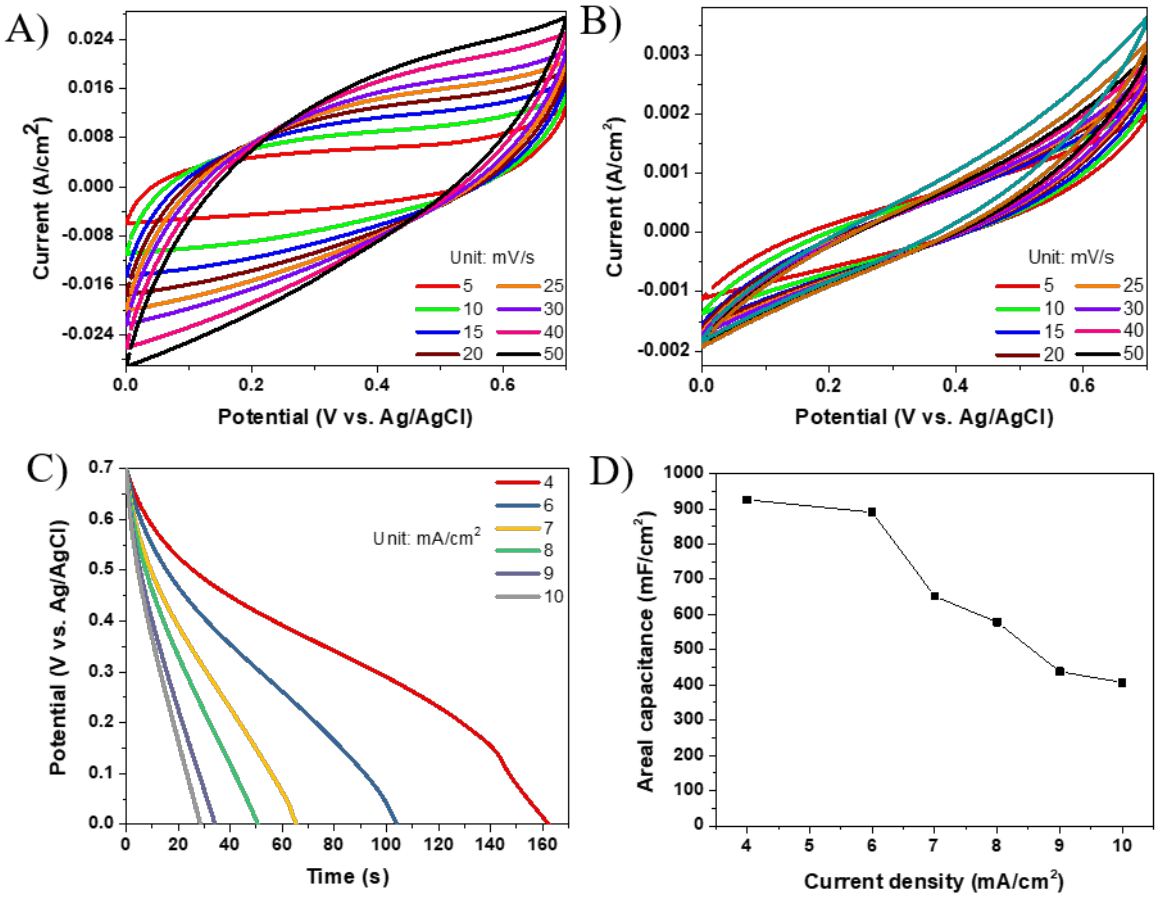

Figure S15. The CV curve of the polypyrrole coated Nickel Foam substrate **NF@PPy** (A) and **PPy/NF@PPy** electrode (B) at 5 mV/s.

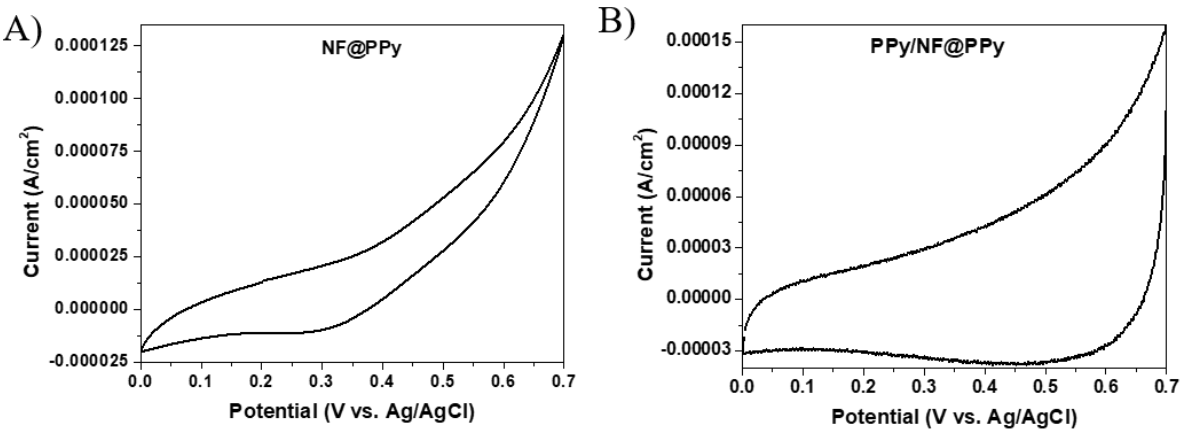

Figure S16. Electrochemical impedance spectra of the working electrodes at different magnifications. Insert: the equivalent electrical circuit.

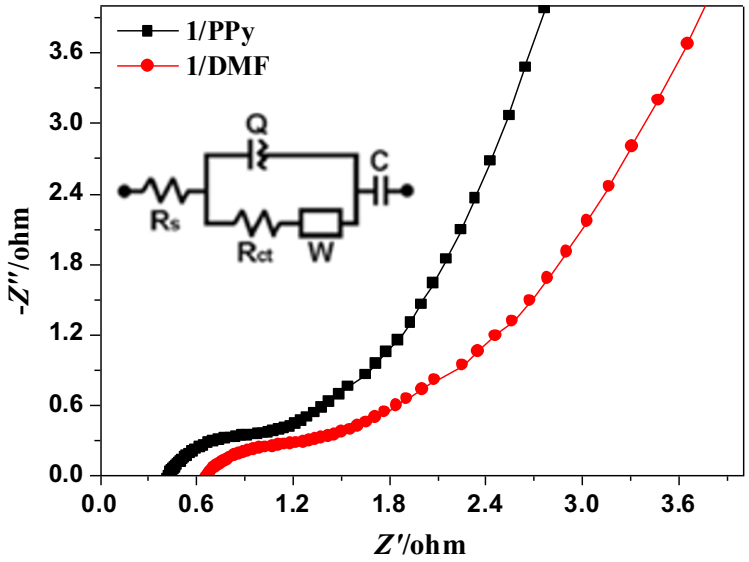

To further understand the fundamental behavior of the supercapacitor electrodes, electrochemical impedance spectroscopy (EIS) measurement was performed for **1/PPy** and **1/DMF** (Figure S15). The spectra were fitted by an equivalent electrical circuit and revealed that both of the equivalent series resistance (R_s) and charge transfer resistance (R_{ct}) of **1 ⊃ PPy** (0.64 and 0.51 ohm, respectively) were slightly smaller than that for **1 ⊃ DMF** (0.82 and 0.63 ohm, respectively). These results indicate again the role of the PPy in enhancing the electrical conductivity of the material.

Each plot is composed of a semicircle at the high to medium frequency region that is assigned to the double layer capacitance C_{dl} and charge transfer resistance (R_{ct}) and a straight line at lower frequencies which corresponds to the Warburg impedance because of the electrolyte and proton diffusion in active materials [12]. The high frequency intercept with the real axis (Z′) represents the equivalent series resistance (R_s), including the ionic resistance of the electrolyte, the intrinsic resistance of active material, and the contact resistance at the interface of the active material/electrolyte interface. To further analyze the charge transfer process within the electrodes, an equivalent electrical circuit and the ZSimpWin software were used to fit the impedance spectra, as shown in the inset of Figure S15a. The R_s of the **1/PPy** electrode was calculated to be 0.64 ohm, which is much smaller than that of **1/DMF** (0.82 ohm). It is well accepted that bigger semicircle means larger R_{ct}, and a higher slope at lower frequencies implies faster diffusion rates [13]. The R_{ct} of **1/PPy** was calculated to be 0.51 ohm, which is relatively lower than the **1/DMF** electrode (0.63 ohm). This fact could be attributed to the presence of conductive PPy in the **MOF-1 ⊃ PPy** hybrids, which acts as an express way for charge transfer, resulting in the improved electrical conductivity [14]. In addition, the new formed open pores and continuous porous architecture of the MOF can be readily filled with

the electrolyte solutions, thus inducing in the improvement of electron/ion transport. The straight line inclining nearly 90º to the real axis in the low-frequency region of the **1/PPy** electrode demonstrates a more effective diffusion of the electrolyte in polymer composite than in the original MOF.

Figure S17. Cycling stability test of the working electrodes at 5 mV/s for 1000 cycles.

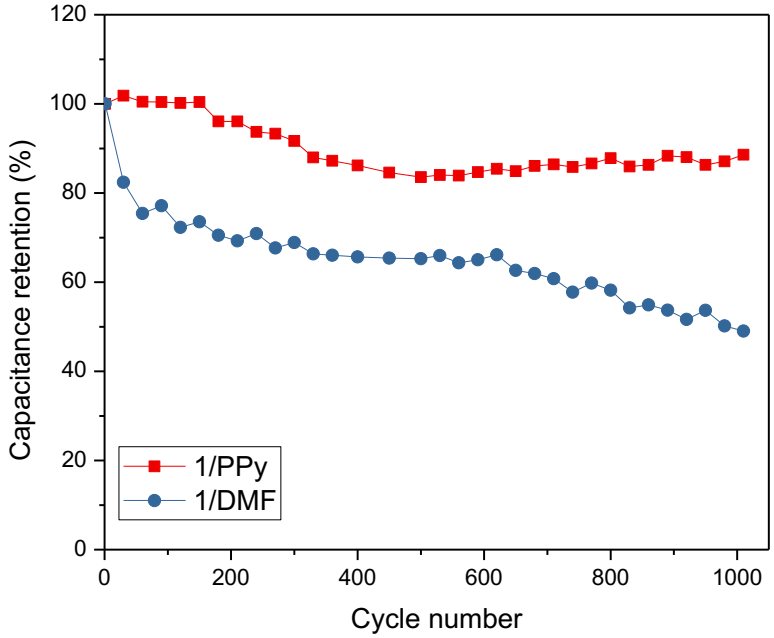

The cycling performance of the as-prepared electrodes was further characterized by CV measurements at a scan rate of 5 mV s^{-1} (Fig. S16). Except for the slightly capacitance loss in the first 350 cycles, the areal capacitance maintained stable from 350 to 500 cycles. In the last 500 cycles, the areal capacitance slightly increased from 811.7 to 864.4 mF/cm^2, corresponding to 88.5% of initial capacitance. No sudden capacitance loss can be observed up to 1000 cycles. On the contrary, the capacitance of **1/DMF** drops sharply in the first 50 cycles and then continuously decreased to 69.5 mF/cm^2 after 1000 cycles, corresponding to 51% of capacitance loss. (Fig. S16). Thus, **1/DMF** shows a much higher capacitance decrease than **1/PPy** after 1000 cycles (51 % against 11.5 %, respectively). Consistent with our working hypothesis, pristine **1** ⊃ **DMF** (Fig. 1) is not stable in the absence of stabilizing DMF or other aromatic solvents.[15] Consequently the electrode containing the later (**1/DMF**) is not stable under the electrochemistry working conditions (Fig. S17).

Figure S18. PXRD patterns of the **1/DMF** (left) and **1/PPy** (right) electrodes at different cycling states.

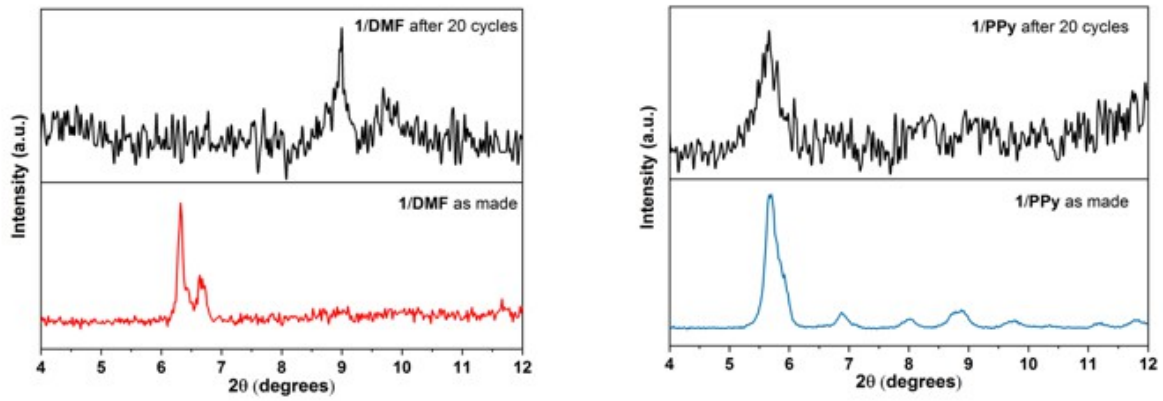

PXRD data of **1/DMF** electrode already shows a displacement of the main diffraction peak to higher angles, which is consistent with the formation of non porous phases [15] (2Θ 8.99 º) after only 20 cycles. On the contrary, and as hypothesized, the MOF is stabilized when incorporates polypyrrole in the structure (**1/PPy**) and consequently, no change is observed in its structure after the same number of cycles.

Table S2. Comparison of **1**/PPy with some reported MOFs- and conductive polymer-based materials.

Materials	**Electrolytes**	**Areal capacitance (mF/cm^2)**	**Cycling stability**	**Ref.**
1/PPy	1 M Na_2SO_4	978.7 at 5 mV/s	88.5% after 1000 cycles	This work
CNT/PANI hydrogel film	1 M H_2SO_4	680 at 1 mA/cm^2	capacitance decreased in the first 300 cycles and increased from 300 to 500 cycles	J. Mater. Chem. A, 2015, 3, 23864–23870
PANI-ZIF-67-CC	3 M KCl	2146 at 10 mV/s	80% after 2000 cycles	J. Am. Chem. Soc. 2015, 137, 4920−4923
ZIF−PPy	1 M Na_2SO_4	225.8 at 0.4 mA/cm^2	90.7% after 10000 times	ACS Appl. Mater. Interfaces 2017, 9, 38737−38744
CNT/PPy	0.5 M H_2SO_4	280 at 1.4 mA/cm^2	95% after 10000 cycles	J. Power Sources, 2015 287, 68-74
PANI/Graphite supercapacitor	1 M H_2SO_4	77.8 at 0.1A/cm^2	83 % after 10000 cycles	Nano Energy, 2013, 2, 1071–1078
SWCNT/Cellulose/PANI	1 M H_2SO_4	330 at 0.2 A/cm^2	79 % after 1000 cycles	Nano Energy, 2015, 11, 568–578
PANI/RGO film	1 M H_2SO_4	718 at 5 mV/s	74 % after 500 cycles	Adv. Funct. Mater. 2014, 24, 2489–2499
PPy/paper	1 M HCl	420 at 1 mA/cm^2	75.6% after 10000 times	Energy Environ. Sci., 2013, **6**, 470-476
nUiO-66 supercapacitor	1.0 M of tetraethylammonium tetrafluoroborate in acetonitrile	1.945 at 0.88 mA/cm^2	capacitance dropped to 80% of the initial value after 7000 cycles	Nano Lett. 2014, 14, 2522−2527
nUiO-67 supercapacitor		0.736 at 0.88 mA/cm^2	after 10000 cycles capacitance decay is less than 20%	
nZIF-8 supercapacitor		0.268 at 0.88 mA/cm^2	capacitance dropped to 80% of the initial value after 2500	
Ti_3C_2/PPy electrode	2 M H_2SO_4	460.5 at 2 mA/cm^2	96% of capacity retention after 10000 cycles	Electrochimica Acta, 2020, 330, 135277.

TaSe2/PPy composites	1 M H_2SO_4	835 at a 2 mV/s	98.7% capacitance retention after 10000 cycles	Nanoscale, 2018, 10, 17341-17346
MXene/BC@PPy hybrid	1 M H_2SO_4	221.21 at 50 mV/s	82.56% retention after 5000 cycles	Nano Energy, 2020, 74, 104812
PPy/cotton-based supercapacitor	PVA/H_2SO_4 gel	481 at 5 mV/s	30% of initial capacitance after 500 cycles	Electrochimica Acta, 2019, 297, 794-804

References

1. M. Y. Tsang, S. Rodríguez-Hermida, K. C. Stylianou, F. Tan, D. Negi, F. Teixidor, C. Viñas, D. Choquesillo-Lazarte, C. Verdugo-Escamilla, M. Guerrero, J. Sort, J. Juanhuix, D. Maspoch and J. Giner Planas, *Crystal Growth & Design*, 2017, **17**, 846-857.
2. C. Lu, T. Ben, S. Xu and S. Qiu, *Angewandte Chemie*, 2014, **53**, 6454-6458.
3. Z. Li, X. Huang, C. Sun, X. Chen, J. Hu, A. Stein and B. Tang, *Journal of Materials Science*, 2016, **52**, 3979-3991.
4. X. Xing, Y. Gui, G. Zhang and C. Song, *Electrochimica Acta*, 2015, **157**, 15-22.
5. L. Wang, X. Feng, L. Ren, Q. Piao, J. Zhong, Y. Wang, H. Li, Y. Chen and B. Wang, *Journal of the American Chemical Society*, 2015, **137**, 4920-4923.
6. X. Xu, J. Tang, H. Qian, S. Hou, Y. Bando, M. S. A. Hossain, L. Pan and Y. Yamauchi, *ACS applied materials & interfaces*, 2017, **9**, 38737-38744.
7. Q. Zhou, Z. Peng, M. Yang, H. Hu, N. Song and L. Ni, *High Performance Polymers*, 2017, **30**, 1267-1275.
8. J. C. Thiéblemont, A. Brun, J. Marty, M. F. Planche and P. Calo, *Polymer*, 1995, **36**, 1605-1610.
9. B. Le Ouay, S. Kitagawa and T. Uemura, *Journal of the American Chemical Society*, 2017, **139**, 7886-7892.
10. T. Uemura, T. Kaseda and S. Kitagawa, *Chemistry of Materials*, 2013, **25**, 3772-3776.
11. B. Le Ouay and T. Uemura, *Israel Journal of Chemistry*, 2018, **58**, 995-1009.
12. J. Cheng, B. Wang, H. L. Xin, C. Kim, F. Nie, X. Li, G. Yang and H. Huang, *Journal of Materials Chemistry A*, 2014, **2**, 2701.
13. M. J. Deng, C. Z. Song, P. J. Ho, C. C. Wang, J. M. Chen and K. T. Lu, *Physical chemistry chemical physics : PCCP*, 2013, **15**, 7479-7483.
14. C. Z. Lai, M. A. Fierke, A. Stein and P. Buhlmann, *Analytical chemistry*, 2007, **79**, 4621-4626.
15. F. Tan, A. Lopez-Periago, M. E. Light, J. Cirera, E. Ruiz, A. Borras, F. Teixidor, C. Vinas, C. Domingo and J. G. Planas, *Advanced materials*, 2018, Adv Mater, 2018, 30, 1800726..